A dataset of microphysical cloud parameters, retrieved from Emission-FTIR spectra measured in Arctic summer 2017

Philipp Richter[1], Mathias Palm[1], Christine Weinzierl[1], Hannes Griesche[2], Penny M. Rowe[3], and Justus Notholt[1]

[1]University of Bremen, Institute of Environmental Physics, Otto-Hahn-Allee 1, 28359 Bremen
[2]Leibniz Institute for Tropospheric Research (TROPOS), Permoserstr. 15, 04318 Leipzig
[3]NorthWest Research Associates, Redmond, WA, USA

Correspondence: Philipp Richter (phi.richter@uni-bremen.de)

Abstract. A dataset of microphysical cloud parameters from optically thin clouds, retrieved from infrared spectral radiances measured in summer 2017 in the Arctic, is presented. Measurements were performed using a mobile Fourier-transform infrared (FTIR) spectrometer which was carried by the RV *Polarstern*. This dataset contains retrieved optical depths and effective radii of ice and water, from which the liquid water path and ice water path are calculated. These water paths and the effective radii are compared with derived quantities from a combined cloud radar, lidar and microwave radiometer measurement synergy retrieval, called Cloudnet. Comparing the liquid water paths from the infrared retrieval and Cloudnet shows significant correlations with a standard deviation of $8.20\,\mathrm{g}\cdot\mathrm{m}^{-2}$. Although liquid water path retrievals from microwave radiometer data come with a uncertainty of at least $20\,\mathrm{g}\cdot\mathrm{m}^{-2}$, a significant correlation and a standard deviation of $5.32\,\mathrm{g}\cdot\mathrm{m}^{-2}$ between the results of clouds with a precipitable water vapour of less than $1\,\mathrm{cm}$ and a liquid water path of at most $20\,\mathrm{g}\cdot\mathrm{m}^{-2}$ retrieved from infrared spectra and results from Cloudnet can be seen. Therefore the comparison with data retrieved from infrared spectra shows that optically thin clouds of the measurement campaign in summer 2017 can be observed well using microwave radiometers within the Cloudnet framework. Apart from this, the dataset of microphysical cloud properties presented here allows to perform calculations of the cloud radiative effects, when the Cloudnet data from the campaign are not available, which was the case from the 22nd July 2017 until the 19th August 2017. The dataset is published at Pangaea (Richter et al., 2021).

1 Introduction

Clouds play an important role in the radiation budget of the earth. In the visible regime, clouds mainly reflect and prevent solar radiation from reaching earth's surface, whereas in the thermal regime clouds prevent surface radiation from escaping to space and re-emit it back to earth, where it warms the surface. A big challenge is the description of optically thin clouds with a liquid water path (LWP) below $100\,\mathrm{g}\cdot\mathrm{m}^{-2}$. In the Arctic, about 80% of the liquid water containing clouds are below this threshold (Shupe and Intrieri, 2004). The change of the broadband surface longwave radiative flux is largest up to a visible optical depth

between 6 to 10 corresponding to a LWP of approximately $40\,\mathrm{g}\cdot\mathrm{m}^{-2}$, depending on the effective droplet radius (Turner et al., 2007).

In the Arctic, a much faster warming than on the rest of the earth takes places, called Arctic amplification. A large number of
25 processes are known to influence the Arctic amplification, but the quantification of each process and its importance is difficult. The project Arctic Amplification: Climate Relevant Atmospheric and Surface Processes and Feedback Mechanisms $(\mathcal{AC})^3$ (Wendisch et al., 2019) aims to close this gap of knowledge by performing various campaigns, model studies and enduring measurements in the Arctic. The measurement campaign presented in this paper is part of $(\mathcal{AC})^3$.

Usually microwave radiometer (MWR) are used for ground-based observations of liquid water clouds. MWR can detect liquid
30 water paths above $100\,\mathrm{g}\cdot\mathrm{m}^{-2}$, also they have the ability to operate continiously 24 hours a day, but LWP retrievals from MWR measurements suffer a high uncertainty in the LWP of at least $15\,\mathrm{g}\cdot\mathrm{m}^{-2}$ (Löhnert and Crewell, 2003). For more accurate observations of optically thin clouds, Fourier Transform Infrared (FTIR) spectrometer can be used. Calibrated FTIR spectrometer are used for the observation of trace gases in absence of the sun or the moon as light source, done for example by Becker et al. (1999) and Becker and Notholt (2000), as well as for the observation of optically thin clouds, performed within the scope of
35 the network of the Atmospheric Radiation Measurement (ARM) using Atmospheric Emitted Radiance Interferometer (AERI) (Knuteson et al. (2004a) and Knuteson et al. (2004b)). Retrievals of infrared radiances from FTIR spectrometers show a smaller uncertainty for cloud parameters of clouds with low amounts of water, but they are not capable to retrieve the water path of optically thick clouds. Therefore, they can be used to supplement existing cloud observation techniques. An emission FTIR spectrometer has been set up on the German research vessel *Polarstern* to perform measurements in summer 2017 in the Arctic
40 around Svalbard.

Lacking freely available physical retrieval algorithms at the time of the measurement campaign, we decided to retrieve microphysical cloud parameters from spectral radiances using the retrieval algorithm Total Cloud Water retrieval (TCWret). TCWret uses the radiative transfer model LBLDIS (Turner, 2005), which includes LBLRTM (Clough et al., 2005) and DISORT (Stamnes et al., 1988). TCWret works on the spectral radiances from $558.5\,\mathrm{cm}^{-1}$ to $1163.4\,\mathrm{cm}^{-1}$, where low absorption
45 of gases occur and therefore the atmosphere is transparent for emissions from clouds. It uses an optimal estimation approach (Rodgers, 2000) and retrieves the liquid water optical depth τ_{liq}, the ice water optical depth τ_{ice} and their respective effective radii r_{liq} and r_{ice}. From this, the LWP and Ice Water Path (IWP) are calculated. The principle of this retrieval technique has been proven already for mixed-phase clouds by the Mixed-phase cloud property retrieval algorithm (MIXCRA) by Turner (2005) and later by the CLoud and Atmospheric Radiation Retrieval Algorithm (CLARRA) by Rowe et al. (2019) and for
50 single-phase liquid clouds using the thermal infrared spectral range (extended line-by-line atmospheric transmittance and radiance algorithm (XTRA) by Rathke and Fischer (2000).

Section 2 describes the measurement area. In section 3 we give an overview of the measurement setup and procedure. In section 4, the ancillary data from radiosondes and ceilometer are introduced. Section 5 describes TCWret including a test with synthetic spectra representative for the Arctic to show the performance of TCWret. Section 6 presents the results of the
55 measurement campaign. After the description of data and code availability, a summary and conclusion is provided.
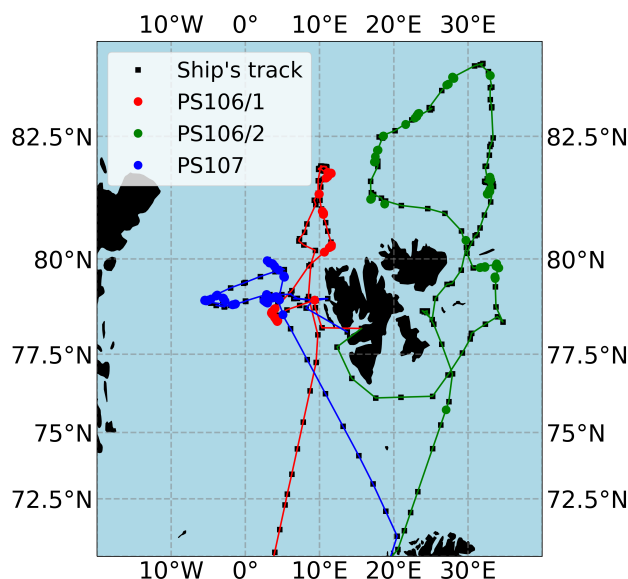
Figure 1. Map of the measurement area. Red markers indicate measurements during PS106.1 (24th May 2017 until 21st June 2017), green markers indicate measurements during PS106.2 (23rd June 2017 until 19th July 2017). Blue markers indicate measurements during PS107 (22nd July 2017 until 19th August 2017).

2 Area of measurements

Measurements were performed around Svalbard in 2017 from the 24th May until the 19th August. The measurements with the FTIR were performed during cruise legs PS106.1 (PASCAL), PS106.2 (SiPCA) and PS107 (FRAM) of the RV *Polarstern*. PS106.1 and PS106.2 are collectively referred to as PS106. For further description see Macke and Flores (2018) and Schewe
60 (2018). Figure (1) shows the positions of the measurement sites and the ship.

3 Measurement setup

Measurements of the atmospheric radiances were performed with a mobile FTIR spectrometer (IFS 55 Equinox by Bruker) in emission mode (without using the sun as light source), which will be from now on referred to as EM-FTIR. The instrument was located in an air-conditioned and insulated container on the A-Deck of RV *Polarstern*. The roof of the container has
65 two openings. Below one opening the EM-FTIR was located. Both openings could be closed in case of precipitation. The interferometer inside the FTIR spectrometer has a movable mirror which gives a maximum optical path difference of $3\,\mathrm{cm}$, which results in a maximum spectral resolution of $\Delta\bar{\nu} = 0.3\,\mathrm{cm}^{-1}$. The spectrometer was permanently rinsed with dry air. Further specifications are described in table (1). A blackbody (SR-80 by CI Systems) was placed manually on the EM-FTIR opening at regular intervals to perform a radiometric calibration.
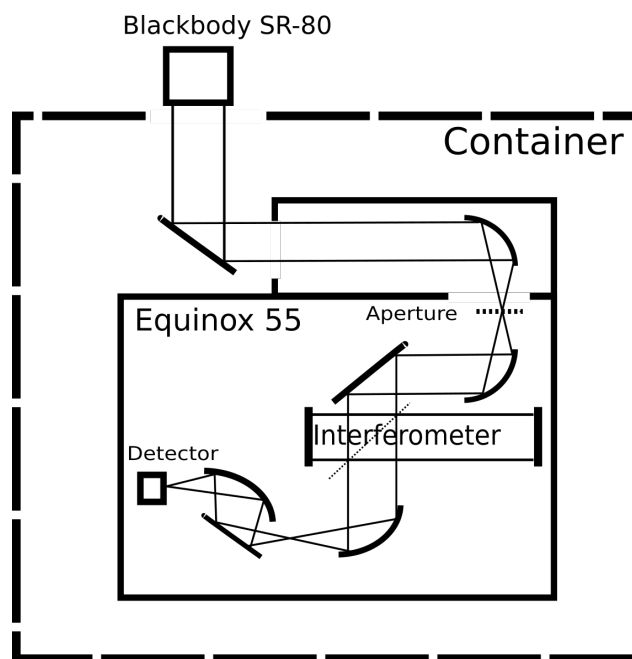
Figure 2. Sketch of the *IFS 55 Equinox*. The blackbody SR-80 can be removed, then atmospheric radiation is measured.

Table 1. Technical specifications of the FTIR spectrometer IFS 55 Equinox.

Beamsplitter	Potassium bromide (KBr)
Detector	Mercury-Cadmium-Tellurium (HgCdT)
Temperature of Detector	Cooled with liquid nitrogen (77 K)
Optical path difference	3 cm
Spectral resolution	$0.3\,\text{cm}^{-1}$
Diameter of entrance arperture	3.5 cm

3.1 Radiometric calibration and emissivity of the blackbody radiation

To obtain the spectral radiance L_{atm}, a radiometric calibration of the EM-FTIR is necessary. To do so, the blackbody radiator SR-80 was used. Its temperature can be set from $-10\,°\text{C}$ to $125\,°\text{C}$ and has an accuracy of $\pm 0.05\,\text{K}$. The radiation by the EM-FTIR is the sum of the radiation of the radiator plus a term which takes into account the temperature of the environment:

$$B = \varepsilon B(T_{BB}) + (1 - \varepsilon)B(T_{lab}) \tag{1}$$
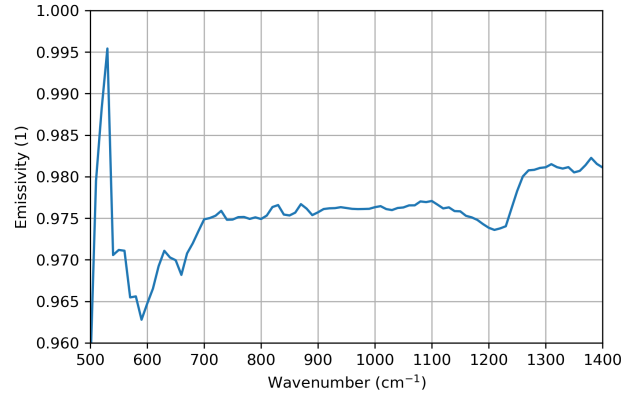
Figure 3. Spectral emissivity of the blackbody radiator.

with the temperature of the blackbody T_{BB} and the temperature of the laboratory T_{lab}, weighted by the blackbody emissivity ε (Revercomb et al., 1988). The spectrally resolved of the emissivity is shown in figure (3). The mean emissivity of the blackbody radiator is $\varepsilon = 0.976$.

The blackbody radiator was either heated up to about $100\,°\mathrm{C}$ or brought to ambient temperature. The radiometric calibration of the spectrometer is performed then using

$$L_{atm} = \varepsilon B_{\bar{\nu}}(T_{amb}) + \varepsilon \frac{B_{\bar{\nu}}(T_{hot}) - B_{\bar{\nu}}(T_{amb})}{\mathcal{F}(I_{hot} - I_{amb})} \cdot \mathcal{F}(I_{atm} - I_{amb}) + (1 - \varepsilon) B_{\bar{\nu}}(T_{lab}) \tag{2}$$

$B(T_{amb,hot,lab})$ are the Planck function of high temperature (T_{hot}), ambient temperature (T_{amb}) and at the temperature of the laboratory (T_{lab}). $I_{hot,amb,atm}$ are the inteferograms of the hot blackbody, blackbody at ambient temperature and the atmospheric measurement. $\mathcal{F}$ is the operator for the Fourier transform. In contrast to the procedere described in Revercomb et al. (1988), here the difference of the interferograms is calculated before applying the Fourier transform.

Spectra of the blackbody radiator are measured at high temperature of $T_{hot} \approx 100\,°\mathrm{C}$ and at ambient temperature T_{amb}. The following cycle was selected for the radiometric calibration: blackbody at T_{hot}, atmospheric radiation, blackbody at T_{amb}, atmospheric radiation, blackbody at T_{hot} and so on. Each measurement cycle of the blackbodies contains 12 individual measurements which are averaged to get one blackbody interferogram I_{hot} or I_{amb}. 40 measurements of atmospheric radiance were performed in each cycle.

3.2 OCEANET measurements and Cloudnet synergistic retrieval

Retrievals of microphysical cloud parameters are compared with results of the synergistic retrieval Cloudnet. The OCEANET-Atmosphere observatory from the Leibniz Institute for Tropospheric Research (TROPOS) in Leipzig (Germany) performed continuous measurements during PS106.1 and PS106.2 (Griesche et al., 2020e). Its container houses a multi-wavelength Raman polarization lidar Polly-XT and a microwave radiometer HATPRO which was complemented during PS106 by a vertically-pointing motion-stabilized 35-GHz cloud radar Mira-35. The OCEANET measurements provide profiles of aerosol and cloud

properties and column-integrated liquid water and water vapor content. To retrieve products like liquid and ice water content the instrument synergistic approach Cloudnet (Illingworth et al., 2007) was applied to these observations. The retrieved Cloudnet dataset during PS106 has been made available via Pangaea (see table 10).

4 Atmospheric profiles and cloud height informations

100 ### 4.1 Cloud ceiling

Informations about the cloud ceiling were recording using a Vaisala Ceilometer CL51 operated by the German Weather Service. The maximum cloud detection altitude is $13\,\mathrm{km}$ with a vertical resolution of $10\,\mathrm{m}$ and a measurement accuracy of $\geq \pm 5\,\mathrm{m}$. Temporal resolution of the results is $60\,\mathrm{s}$. Although only data of the cloud base height is given, it was decided to use these data instead of the Cloudnet height profile, because the ceilometer data was available during the entire cruise, whereas the Cloudnet

105 measurements were only available for the PS106. Without changing the input data, a consistent dataset for the retrieval should be created. Data are available at Schmithüsen (2017a), Schmithüsen (2017b) and Schmithüsen (2017c).

4.2 Radiosounding

Radiosondes were launched four times per day (00 UTC, 06 UTC, 12 UTC, 18 UTC) during the PS106 and twice per day (06 UTC and 12 UTC) during the PS107 (Schmithüsen (2017d), Schmithüsen (2017e) and Schmithüsen (2017f)). Data were

110 measured using a RS92 radiosonde by Vaisala. Data of air pressure, temperature, relative humidity, wind speed and wind direction were recorded. Accuracies are $0.5\,\mathrm{K}$ for temperature measurements, $5\,\%$ for relative humidity and $1\,\mathrm{hPa}$ for air pressure. Wind speed and wind direction are not used here. Atmospheric profiles between two radiosonde launches are acquired by linear interpolation. If the radiosonde stopped measurements before reaching $30\,\mathrm{km}$, data were extended using the ERA5 reanalysis (Hersbach et al., 2018).

115 ## 5 Total Cloud Water retrieval (TCWret)

Total **C**loud **W**ater **ret**rieval (TCWret) is a retrieval algorithm for microphysical cloud parameters from FTIR spectra. It is inspired by MIXCRA (Turner, 2005) and XTRA (Rathke and Fischer, 2000) and uses an optimal estimation approach (Rodgers, 2000) to invert the measured spectral radiances for retrieving microphysical cloud parameters.

5.1 Radiative Transfer Models

120 Two radiative transfer models are used in TCWret: the Line-By-Line Radiative Transfer Model (LBLRTM) (Clough et al., 2005) and the DIScrete Ordinate Radiative Transfer model (DISORT) (Stamnes et al., 1988). DISORT is called by LBLDIS (Turner, 2005) to calculate spectral radiances.
LBLRTM calculates the optical depth for gaseous absorbers and the water vapour continuum. The profiles of H_2O, CO_2,

O_3, CO, CH_4 and N_2O either can be set by the user, or a predefined atmosphere of LBLRTM can be used. A subarctic
summer atmosphere, implemented in LBLRTM, has been used for all gases except H_2O, which has been read from radiosonde
measurements.

DISORT calculates the monochromatic radiative transfer through an vertically inhomogenious plane-parallel medium including
scattering, absorption and emission. DISORT provides the spectral radiances under given single-scatter parameters.

LBLDIS takes over the calculated optical depths from LBLRTM. Additonally, LBLDIS comes with several databases of single-
scatter parameters for liquid water and ice (Turner, 2014). These databases contain extinction cross sections, absorption cross
sections, scattering cross sections, single-scatter albedo, asymmetry factor and phase functions for different wavenumber and
effective radii. Refractive indices for liquid water droplets and ice crystals are taken from Downing and Williams (1975) and
Warren (1984) respectively. Temperature depended refractive indices for liquid water are from Zasetsky et al. (2005). However,
it is important to note that they have large uncertainties from $1000\,\mathrm{cm}^{-1}$ to $1300\,\mathrm{cm}^{-1}$ (Rowe et al., 2013). Scattering properties
for more complex ice particle shapes like aggregates, bullet rosettes, droxtals, hollow columns, solid columns, plates and
spheroids were calculated by Yang et al. (2001) using a combination of Finite Difference Time Domain (FDTD), geometric
optics and Mie theory.

The droplet size distributions follow a gamma size distribution. The gamma size distributions were chosen is a way, that they
fit to the data during the First International Satellite Cloud Climatology Project (ISCCP) Regional Experiment (FIRE) Arctic
Cloud Experiment (ACE). For further details, please refer to Turner et al. (2003).

5.2 Working principle of TCWret

TCWret retrieves optical depths of liquid water and ice water and the effective radii of liquid water droplets and ice crystals from
infrared spectral radiances. The retrieval of microphysical cloud parameters is a nonlinear problem, so an iterative algorithm is
needed:

$$\boldsymbol{x}_{n+1} = \boldsymbol{x}_n + \boldsymbol{s}_n \tag{3}$$

Here $\boldsymbol{x_n}$ and $\boldsymbol{x_{n+1}}$ are the state vectors containing cloud parameters of the n-th and $(n+1)$-th step and $\boldsymbol{s_n}$ is the modification
of the cloud parameters during the n-th iteration. The governing equation to determine $\boldsymbol{s_n}$ is

$$\left(\mathbf{K}_n^T \mathbf{S_y}^{-1}\mathbf{K}_n + \mathbf{S_a}^{-1} + \mu^2 \mathbf{S_a}^{-1}\right)\boldsymbol{s}_n = \mathbf{K}_n^T \mathbf{S_y}^{-1}\left[\boldsymbol{y} - F(\boldsymbol{x}_n)\right] + \mathbf{S_a}^{-1}\cdot(\boldsymbol{x_a} - \boldsymbol{x}_n) \tag{4}$$

. The quantities in the equation are the jacobian matrix $\mathbf{K} = \left(\frac{\partial F(x_i)_j}{\partial x_i}\right)$, the inverse of the variance-covariance matrix $\mathbf{S_y}^{-1}$,
the a priori $\boldsymbol{x_a}$ of the cloud parameters and the inverse covariances of the a priori $\mathbf{S_a}^{-1}$, the measured spectral radiances $\boldsymbol{y}$, the
calculated spectral radiances $F(\boldsymbol{x_n})$ and the Levenberg-Marquardt term $\mu^2 \cdot \mathbf{S_a}^{-1}$.

The aim of the iterations is to minimize the cost function $\xi^2(\boldsymbol{x})$.

$$\xi^2(\boldsymbol{x}_n) = \left[\boldsymbol{y} - F(\boldsymbol{x}_n)\right]^T \mathbf{S_y}^{-1}\left[\boldsymbol{y} - F(\boldsymbol{x}_n)\right] + \left[\boldsymbol{x_a} - \boldsymbol{x}_n\right]^T \mathbf{S_a}^{-1}\left[\boldsymbol{x_a} - \boldsymbol{x}_n\right] \tag{5}$$

Table 2. Microwindows used in TCWret to retrieve the microphysical cloud parameters of this dataset.

Interval (cm^{-1})
$558.5 - 562.0$
$571.0 - 574.0$
$785.9 - 790.7$
$809.5 - 813.5$
$815.3 - 824.4$
$828.3 - 834.6$
$842.8 - 848.1$
$860.1 - 864.0$
$872.2 - 877.5$
$891.9 - 895.8$
$898.2 - 905.4$
$929.6 - 939.7$
$959.9 - 964.3$
$985.0 - 991.5$
$1092.2 - 1098.1$
$1113.3 - 1116.6$
$1124.4 - 1132.6$
$1142.2 - 1148.0$
$1155.2 - 1163.4$

Convergence is reached, if the change of the cost function is below a given threshold, here set to 0.1%:

155
$$\frac{\xi^2(x_{n+1}^2) - \xi^2(x_n)}{\xi^2(x_{n+1})} < 0.001 \tag{6}$$

However, convergence in the sense of the cost function does not necessarily mean that the fitted and measured spectrum match. For example, the step size parameter of the Levenberg-Marquardt method could be so large that the cost function changes little. Then the convergence criterion is fulfilled, but the fit does not agree with the measurement. To identify these cases, a

reduced-ξ^2-test is performed. This test is used to calculate the distance between calculated and measured radiance, taking into account the variance of the spectrum σ^2. It is defined as

$$\xi^2_{reduced} = DOF \cdot \sum_{n=1}^{N} \frac{y(\bar{\nu}_n) - F(x, \bar{\nu}_n)}{\sigma^2} \tag{7}$$

with DOF = number of datapoints - number of parameters. As empirical values, we assume all retrievals with $\xi^2_{reduced} < 1.0$ as converged correctly. Results with $\tau_{liq} + \tau_{ice} > 6$ are excluded.

As we do not necessarily have prior informations about the optical depths and effective radii, we decided to set the covariance of the a priori to large values. This shall ensure that the chosen a priori does not constrain the retrieval too strong. Initial values and a priori are set to equal values: $\boldsymbol{x} = (0.25, 0.25, \log(5.0), \log(20.0))$. The logarithm was chosen so that all entries of $\boldsymbol{x}$ have similar size. The variance-covariance matrix of the a priori is set to

$$\mathbf{S_a}^{-1} = \begin{pmatrix} 0.04 & 0 & 0 & 0 \\ 0 & 0.04 & 0 & 0 \\ 0 & 0 & 0.047 & 0 \\ 0 & 0 & 0 & 0.047 \end{pmatrix} \tag{8}$$

. Variances in $\mathbf{S_y}^{-1}$ are calculated from the spectral region between $1925\,\mathrm{cm}^{-1}$ and $2000\,\mathrm{cm}^{-1}$, where no signal from the atmosphere is expected. The variance-covariance matrix is assumed to be diagonal: $\mathbf{S_y} = \sigma^2 \mathbf{I}$. It is assumed to be the variance of the scene. To retrieve cloud parameters, only radiance from spectral intervals given in table (2) is used.

5.3 Products of TCWret

Direct retrieval products are τ_{liq}, τ_{ice}, r_{liq} and r_{ice}. From these parameters the water paths are calculated:

$$LWP = \frac{2}{3} \cdot r_{liq} \cdot \tau_{liq} \cdot \varrho_{liq} \tag{9}$$

$$IWP = \frac{N \cdot V_0(r_{ice}) \cdot \tau_{ice}}{\sigma_{ice}} \cdot \varrho_{ice} \tag{10}$$

with the volumetric mass densities of liquid water $\varrho_{liq} = 1000\,\mathrm{kg \cdot m^{-3}}$, ice water $\varrho_{ice} = 917\,\mathrm{kg \cdot m^{-3}}$, the particle number density N and the extincion coefficient $\sigma_{ice} = ext(r_{ice}) \cdot N$. The total volume of an ice crystal $V_0(r_{ice})$ and the extinction cross section of an ice droplet $ext(r_{ice})$, both integrated over the gamma size distribution are read from the databases of single-scattering parameters. The formula for the liquid water path works for spherical droplet only, while the formula for the ice water path is valid for ice crystals of any shape (Turner, 2005).

5.4 Covariance matrix and averaging kernels

Retrieval errors are calculated from the variance-covariance matrix $\mathbf{S}_r$ of the retrieval. It is calculated by

$$\mathbf{S}_r = \mathbf{T}_r \mathbf{S}_y \mathbf{T}_r^T \tag{11}$$

. The index r denotes quantities of the final iteration. The retrieval uses a Levenberg-Marquardt algorithm, therefore the variance-covariance matrix and the transfer matrix $\mathbf{T}$ are calculated iteratively, as described by Ceccherini and Ridolfi (2010). In brief: In each step the transfer matrix $\mathbf{T}$ is calculated taking into account the current step size parameter μ by

$$
\begin{cases}
\mathbf{T_0} = \mathbf{0} \\
\mathbf{T}_{i+1} = \mathbf{G}_i + \left(\mathbf{I} - \mathbf{G}_i \mathbf{K}_i - \mathbf{M}_i \mathbf{S}_a^{-1} \right) \mathbf{T}_i
\end{cases}
\tag{12}
$$

with $\mathbf{0}$ as zero matrix and $\mathbf{I}$ as identity matrix. $\mathbf{M}_i$ is the term in the brackets on the left side of (4) and $\mathbf{G}_i = \mathbf{M}_i \mathbf{K}_i^T \mathbf{S}_y^{-1}$. Diagonal elements of $\mathbf{S}_r$ are the variances of the final cloud parameters.

Another important quantity to characterize the retrieval quality is the Averaging Kernel Matrix $\mathbf{A}$. The averaging kernel matrix contains the derivatives of the retrieved quantities with respect to the true state vector

$$
\mathbf{A} = \frac{\partial \boldsymbol{x_r}}{\partial \boldsymbol{x_t}}
\tag{13}
$$

. where $\boldsymbol{x_r}$ means the retrieved parameters and $\boldsymbol{x_t}$ are the unknown true parameters. On the diagonal elements one finds the derivatives of each element in the retrieved state vector with respect to its corresponding element in the true state vector. The trace of the averaging kernel matrix gives the degrees of freedom of the signal, which can be interpreted as the number of individually retrievable parameters from the measurement (Rodgers, 2000). The averaging kernel matrix sets the retrieval and the a priori into context:

$$
\boldsymbol{x_r} = \boldsymbol{x_a} + \mathbf{A}(\boldsymbol{x_t} - \boldsymbol{x_a})
\tag{14}
$$

From this relationship it can be seen that in the optimal case the Averaging Kernel Matrix is the unit matrix. Smaller entries mean a stronger influence by the a priori. Averaging kernels in TCWret are calculated via

$$
\mathbf{A} = \mathbf{T}_r \mathbf{K}_r
\tag{15}
$$

(Ceccherini and Ridolfi, 2010). Errors of LWP and IWP are calculated from error propagation:

$$
\sigma_Y = \pm \sqrt{ \sum_i \left(\frac{\partial Y}{\partial m_i} \sigma_{m_i} \right)^2 }
\tag{16}
$$

where Y is either LWP or IWP, $\frac{\partial Y}{\partial m}$ is the partial derivative of Y with respect to an atmospheric parameter $m = \{\tau_{liq}, \tau_{ice}, r_{liq}, r_{ice}\}$ and σ_{m_i} is the variance of the i-th parameter m_i.

5.5 Retrieval performance

A set of synthetic testcases containing spectral radiances of artifical clouds with known cloud parameters, created by Cox et al. (2016), will be used to test the ability of TCWret to retrieve $\tau_{liq}, \tau_{ice}, r_{liq}$ and r_{ice}. Additionally, the derived quantities LWP and IWP are discussed. This dataset contains several representative cases of Arctic clouds. Clouds are set to be

Table 3. Results of the testcase retrievals. $|r|$ is the correlation coefficient of each quantity. Mean is the mean difference between retrieval and the true size of the parameter. STD (TC) is the standard deviation of the difference between retrieval and true parameter. ERR (OE) is the standard deviation provided by the optimal estimation without covariances ($\tau_{liq,ice}, r_{liq,ice}$) or the standard deviation from propagation of uncertainty using the variances (LWP, IWP, τ_{cw}, f_{ice}, $\bar{r}$).

Quantity	$|r|$	Mean	STD (TC)	ERR (OE)	Maximum in testcases
τ_{liq} (1)	0.86	-0.08	0.52	0.34	5.45
τ_{ice} (1)	0.78	0.19	0.56	0.32	4.45
$\tau_{cw} = \tau_{liq} + \tau_{ice}$ (1)	0.99	0.11	0.17	0.67	5.94
f_{ice} (1)	0.70	0.08	0.25	0.59	1.00
r_{liq} (µm)	0.59	-2.37	3.35	2.93	22.00
r_{ice} (µm)	0.65	2.94	9.68	2.39	70.00
$\bar{r} = (1 - f_{ice}) \cdot r_{liq} + f_{ice} \cdot r_{ice}$ (µm)	0.80	1.75	5.75	14.30	56.82
LWP ($\mathrm{g \cdot m^{-2}}$)	0.68	-1.85	6.01	2.31	46.90
IWP ($\mathrm{g \cdot m^{-2}}$)	0.82	1.91	9.85	5.06	107.39

either vertically homogenous, topped by a layer of liquid water or with thin boundaries. Ice crystal shapes are mostly set to be spheres, but some cases where calculated with hollow columns, solid columns, bullet rosettes or plates. All spectra are convoluted with a sinc-function to the resolution of the IFS 55 Equinox ($0.3\,\mathrm{cm^{-1}}$) and perturbed by a Gaussian distributed noise of $1\,\mathrm{mW \cdot (sr \cdot cm^{-1} \cdot m^{-2})^{-1}}$: We modified the spectral radiance at each wavenumber by drawing a random number from a normal distribution with the true spectral radiance as mean of the distribution and $1\,\mathrm{mW \cdot (sr \cdot cm^{-1} \cdot m^{-2})^{-1}}$ as its standard deviation. This value has been chosen, because it is near the observed standard deviation of the real spectra from the measurement campaign of $0.82\,\mathrm{mW \cdot (sr \cdot cm^{-1} \cdot m^{-2})^{-1}}$. Ice crystals are chosen to be spheres, thus only the testcases which are calculated with spherical ice crystals are used here. The influence of the chosen ice particle form will be adressed later.

Table (3) gives the correlation coefficients, mean deviations and standard deviations between the retrieved cloud parameters of the testcases and the true cloud parametern. Additionally, the stndard deviation calculated via the variance-covariance matrix is given. In all cases, a significant correlation can be observed. This means, TCWret can retrieve all of the parameters from the testcases under the given uncertainties.

Of all direct retrieval products, the optical depths τ_{liq} and τ_{ice} have the highest agreement to the true cloud parameters. For the liquid phase, the difference to the true optical depths is (-0.08 ± 0.52). For the optical depth of the ice phase, the difference is larger with (0.19 ± 0.56). Since τ_{liq} and τ_{ice} include both optical depths and phase, the optical depth of the condensed water $\tau_{cw} = \tau_{liq} + \tau_{ice}$ as well as the fraction of ice in the optical depth $f_{ice} = \tau_{ice} \cdot \tau_{cw}$ are calculated. Here it becomes clear that the

optical depth can be determined accurately ($|r| = 0.99$, mean and standard deviation (0.11 ± 0.17)). It then also follows that the deviations of τ_{liq} and τ_{ice} come from the phase determination. The deviation for the phase is (0.08 ± 0.25) with a correlation coefficient of $|r| = 0.70$.

When considering the effective radii, only results of r_{liq} were used in where f_{ice} is less than 0.9. For r_{ice} only results
230 with $f_{ice} > 0.1$ are considered. The mean difference of the retrieval from the true parameters is the standard deviations are (-2.37 ± 3.35) for r_{liq} and (2.94 ± 9.68) for r_{ice}. Additionally, the quantity $\bar{r} = (1 - f_{ice}) \cdot r_{liq} + f_{ice} \cdot r_{ice}$ is calculated. It can be interpreted as the mean effective radius for liquid droplets and ice crystals of the entire cloud. For $\bar{r}$, the difference to the testcases is $(1.75 \pm 5.75)\,\mu m$ with a correlation coefficient of $|r| = 0.80$. Therefore, $\bar{r}$ can be estimated independently from its constituents r_{liq}, r_{ice} and f_{ice}. For example, a too large r_{ice} can lead to an underestimation of r_{liq} and vice versa.

235 The mean averaging kernel matrix over all retrievals is

$$
\mathbf{A} = \begin{pmatrix}
0.87 & 0.09 & -0.15 & -0.09 \\
0.11 & 0.90 & 0.19 & 0.03 \\
-0.04 & 0.07 & 0.50 & 0.05 \\
-0.16 & 0.05 & 0.03 & 0.42
\end{pmatrix}
\tag{17}
$$

The top two rows belong to τ_{liq} and τ_{ice}, the bottom two rows belong to r_{liq} and r_{ice}. From equation (14) can be seen that the diagonal elements show for each parameter how strong the retreived parameter is influenced by the a priori. Whereas the diagonal elements of the optical depths are near 1, indicating independence from the a priori, results for r_{liq} and r_{ice} show
240 a larger influence from the a priori. From the trace of the averaging kernels follow 2.69 degrees of freedom of the signal. Therefore, additional information that limits the number of independent quantities to be determined can improve the retrieval. The water paths are calculated from the optical depths and effective radii, therefore both quantities are influenced by the phase determination, as seen before in $\tau_{liq,ice}$ and $r_{liq,ice}$. The difference from the testcases is (-1.85 ± 6.01) for the LWP and (1.91 ± 9.85) for the IWP. However, the standard deviation for the LWP is less than the standard deviation observed for LWP
245 from microwave radiometer of at least $15\,g \cdot m^{-2}$ (Löhnert and Crewell, 2003).

Standard devations given by the variance-covariance matrix of the retrieval are shown in table (3) and named as ERR(OE). ERR(OE) is below STD(TC) for $\tau_{liq,ice}$, $r_{liq,ice}$, LWP and IWP. This might be due to uncertainties from the forward model, which are neglected here, propagated into the retrievals or due to the assumption of a diagonal variance matrix $\mathbf{S_y}$. To address the effect of these differences in the uncertainties, ERR(OE) is scaled so it matches STD(TC).

250 ## 5.6 Erorrs of atmospheric profile and calibration

For estimating the propagation of errors of the humidty profile, cloud temperature and emissivity and temperature of the blackbody radiator into the cloud parameters, cloud parameters from the testcases have been retrieved. In contrast to the section of the retrieval performance, following modifications were perfomed:

– Increase cloud temperature by $1\,K$

255 – Increase atmospheric humidity by $10\,\%$

Table 4. Standard deviations of the differences between retrievals without parameter errors and retrievals with parameter errors.

Quantity	σ_T	σ_q	σ_L
τ_{liq} (1)	0.31	0.03	0.07
τ_{ice} (1)	0.32	0.02	0.08
r_{liq} (µm)	2.14	0.27	3.33
r_{ice} (µm)	5.23	1.00	15.76
LWP (g · m^{-2})	2.84	0.25	1.35
IWP (g · m^{-2})	5.64	0.64	3.11
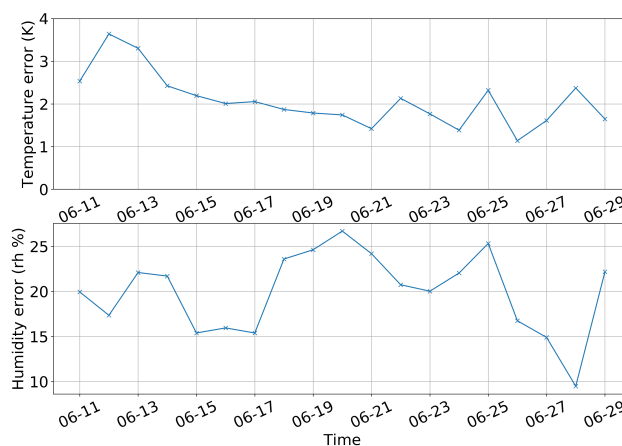
Figure 4. Combined device error and interpolation error.

  – Increase radiance by $2\,\mathrm{mW} \cdot (\mathrm{cm}^{-1} \cdot \mathrm{m}^2 \cdot \mathrm{sr})^{-1}$

These errors will be called *parameter errors*. Each of these modifications is applied individually, creating three new datasets. To separate the influence of the parameter errors from the retrieval performance, the results of the parameter error-data are compared to the dataset calculated by TCWret to determine the retrieval performance instead of the true cloud parameters. For each testcase, the difference between the retrieval results with parameter error and without parameter error is determined. As an estimate of the error of each atmospheric parameter, the standard deviation of all differences is calculated. The standard deviations per unit size are shown in table (4). Then, the parameter error is

$$\Delta par = \pm\sqrt{(\sigma_T \Delta T)^2 + (\sigma_q \Delta q)^2 + (\sigma_L \Delta L)^2} \tag{18}$$

with the cloud temperature T, the relative humidity q, the radiance L and their errors ΔT, Δq and ΔL. Device errors of the radiosonde are $\Delta T = 0.5\,\mathrm{K}$ and $\Delta q = 5\,\%$. Additionally, the error introduced with the linear interpolation of the temperature and relative humidity must be estimated. To estimate this interpolation error, the interpolated profile is compared with the vertical profile of the corresponding variables of the ERA5 reanalysis. The standard deviation of the difference of the profiles is interpreted as the interpolation error. Figures (4) gives the combined device error and interpolation error, as an example for the period from 11th June 2017 to 30th June 2017.

The accuracy of the blackbody temperature and emissivity are $\Delta T_{BB} = \pm 0.05\,\mathrm{K}$ and $\Delta\epsilon = \pm 0.02$. The propagation of these errors into the radiance is performed by

$$\Delta L = \sqrt{\left(\frac{\partial L_{atm}}{\partial \epsilon} \cdot 0.02\right)^2 + \left(\frac{\partial L_{atm}}{\partial T_{BB}} \cdot 0.05\,\mathrm{K}\right)^2} \tag{19}$$

To estimate $\frac{\partial L_{atm}}{\partial \epsilon}$, a spectrum is calibrated with an emissivity of ε' and $\varepsilon' + h$. The differential quotient is calculated by $\frac{\partial L_{atm}}{\partial \epsilon} = \frac{L(\varepsilon'+h)-L(\varepsilon')}{h}$ with the $L(\varepsilon')$ as the radiance under the emissivity ε'. From $\epsilon = 0.975$ and $h = 0.02$ follows $\frac{\partial L_{atm}}{\partial \epsilon} \cdot 0.02 = -0.98\,\mathrm{mW} \cdot (\mathrm{sr} \cdot \mathrm{cm}^{-1} \cdot \mathrm{m}^2)^{-1}$. The second differential quotient $\frac{\partial L_{atm}}{\partial T_{BB}}$ is estimated using equation (2). The emissivity is set to 1. The measured radiance of the hot blackbody is larger than the radiance of the atmosphere ($\mathcal{F}(I_{hot}) > \mathcal{F}I_{atm}$) and therefore the quotient $\frac{\mathcal{F}(I_{hot}-I_{amb})}{\mathcal{F}(I_{atm}-I_{amb})} < 1$. Setting $\frac{\mathcal{F}(I_{hot}-I_{amb})}{\mathcal{F}(I_{atm}-I_{amb})} = 1$ as an upper limit, equation (2) can be written as $L = B_{\bar{\nu}}(T_{hot})$. Thus, the estimation of the radiance error caused by temperature uncertainties depends on the temperature of the hot blackbody. With $T_{BB} = T_{hot} = 100\,\mathrm{K}$ is $\frac{\partial L_{atm}}{\partial T_{BB}} \cdot 0.05 = 0.10\,\mathrm{mW} \cdot (\mathrm{sr} \cdot \mathrm{cm}^{-1} \cdot \mathrm{m}^2)^{-1}$ as an average for the spectral interval between $500\,\mathrm{cm}^{-1}$ and $2000\,\mathrm{cm}^{-1}$. This gives $\Delta L = 0.99\,\mathrm{mW} \cdot (\mathrm{sr} \cdot \mathrm{cm}^{-1} \cdot \mathrm{m}^2)^{-1}$. Setting $\Delta T = 2\,\mathrm{K}$, $\Delta q = 17.5\,\%$ and $\Delta L = 0.99\,\mathrm{mW} \cdot (\mathrm{sr} \cdot \mathrm{cm}^{-1} \cdot \mathrm{m}^2)^{-1}$ gives $\Delta\tau_{liq} = 0.82$, $\Delta\tau_{ice} = 0.77$, $\Delta r_{liq} = 7.21\,\mu\mathrm{m}$, $\Delta r_{ice} = 25.63\,\mu\mathrm{m}$, $\Delta LWP = 7.27\,\mathrm{g} \cdot \mathrm{m}^{-2}$ and $\Delta IWP = 16.21\,\mathrm{g} \cdot \mathrm{m}^{-2}$.

5.7 Results for different ice particle shapes

Without the ability to retrieve the ice shape from the spectral radiances, the data from the measurement campaign is used to investigate the choice of the ice crystal shape on the retrieval results. Table (5) shows the standard deviations of r_{ice} for various ice crystal shapes. In particular, the retrievals with bullet rosettes and plates strongly deviate from the other results. The standard deviation for bullet rosettes is always above that of the test cases. For plates, it is only lower with aggregates, at $9.50\,\mathrm{g} \cdot \mathrm{m}^{-2}$. From this it can be concluded that an incorrect choice of ice shape causes a particularly large error if the ice crystals are of the shape bullet rosette or plate or if the retrieval incorrectly uses bullet rosette or plate although the ice crystals have a different shape.

Unlike r_{ice}, τ_{ice} is less strongly influenced by the ice crystal shape. Results for τ_{ice} are shown in table (7). Largest standard deviation occurs in the cases of bullet rosettes and aggregates.

In table (6) are the standard deviations for the differentials of IWP with different ice crystal shapes. Again, the standard deviations for bullet rosettes and plates are larger than for the other ice particle shapes. The standard deviation of $9.85\,\mathrm{g} \cdot \mathrm{m}^{-2}$ calculated from the testcases is not exceeded in any case. Thus, the IWP is less susceptible to an incorrectly chosen ice crystal

Table 5. Standard deviations for the difference of r_{ice} with different ice crystal shapes. Shapes are spheres (SPH), aggregates (A), bullet rosette (BR), droxtals (D), hollow columns (HC), plates (P), solid columns (SC) and spheroids (SPO). Bold numbers show standard deviations which exceed the standard deviation of r_{ice} from the testcases ($9.68\,\mu m$).

	SPH	A	BR	D	HC	P	SC	SPO
SPH		6.76	**14.15**	4.17 4.62	**10.72**	3.88	3.18	
A	6.76		**12.14**	6.76	5.60	9.50	6.58	6.86
BR	**14.15**	**12.14**		**13.78**	**12.89**	**14.52**	**13.45**	**13.84**
D	4.17	6.76	**13.78**		4.78	**10.88**	2.99	3.67
HC	4.62	5.60	**12.89**	4.78		**10.19**	4.47	4.52
P	**10.72**	9.50	**14.52**	**10.88**	**10.19**		**10.84**	**11.07**
SC	3.88	6.58	**13.45**	2.99	4.47	**10.84**		3.56
SPO	3.18	6.86	**13.84**	3.67	4.52	**11.07**	3.56	

Table 6. Standard deviations for the difference of IWP with different ice crystal shapes. Shapes are spheres (SPH), aggregates (A), bullet rosette (BR), droxtals (D), hollow columns (HC), plates (P), solid columns (SC) and spheroids (SPO). Bold numbers show standard deviations which exceed the standard deviation of IWP from the testcases ($9.85\,g\cdot m^{-2}$).

	SPH	A	BR	D	HC	P	SC	SPO
SPH		7.58	9.31	4.37	6.00	7.80	3.90	3.39
A	7.58		8.32	7.08	6.80	7.29	7.04	7.79
BR	9.31	8.32		9.13	8.85	9.13	9.08	9.72
D	4.37	7.08	9.13		6.49	7.37	4.20	4.93
HC	6.00	6.80	8.85	6.49		8.04	6.27	5.71
P	7.80	7.29	9.13	7.37	8.04		6.99	8.45
SC	3.90	7.04	9.08	4.20	6.27	6.99		4.43
SPO	3.39	7.79	9.72	4.93	5.71	8.45	4.43	

shape than r_{ice}. This can also be deduced from equation (10), since in addition to r_{ice}, τ_{ice} is also included in the calculation of the IWP, which reacts less strongly to the shape of the ice crystals than r_{ice}.

Table 7. Standard deviations for the difference of τ_{ice} with different ice crystal shapes. Shapes are spheres (SPH), aggregates (A), bullet rosette (BR), droxtals (D), hollow columns (HC), plates (P), solid columns (SC) and spheroids (SPO). Bold numbers show standard deviations which exceed the standard deviation of τ_{ice} from the testcases (0.56).

	SPH	A	BR	D	HC	P	SC	SPO
SPH		0.49	**0.57**	0.39	0.38	0.49	0.36	0.30
A	0.49		0.39	0.43	0.41	0.36	0.41	0.47
BR	**0.57**	0.39		0.51	0.47	0.37	0.52	0.55
D	0.39	0.43	0.51		0.41	0.46	0.37	0.40
HC	0.38	0.41	0.47	0.41		0.42	0.37	0.36
P	0.49	0.36	0.37	0.46	0.42		0.41	0.48
SC	0.36	0.41	0.52	0.37	0.37	0.41		0.36
SPO	0.30	0.47	0.55	0.40	0.36	0.48	0.36	
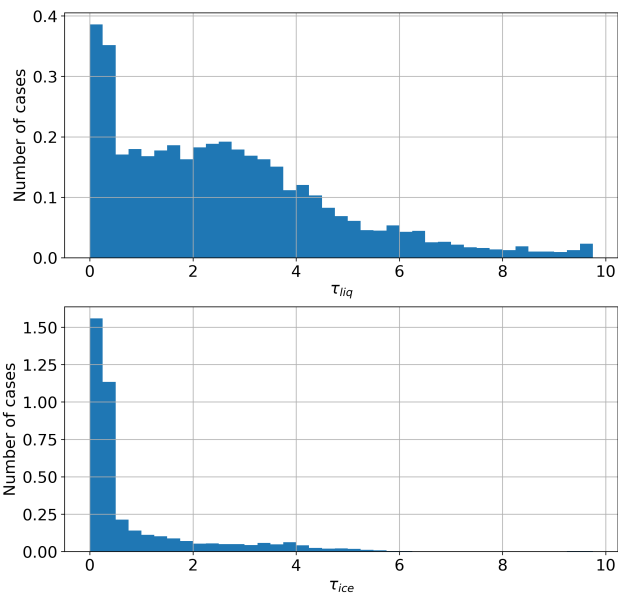
Figure 5. Distribution of retreived optical depths for liquid water (upper plot) and ice water (lower plot).
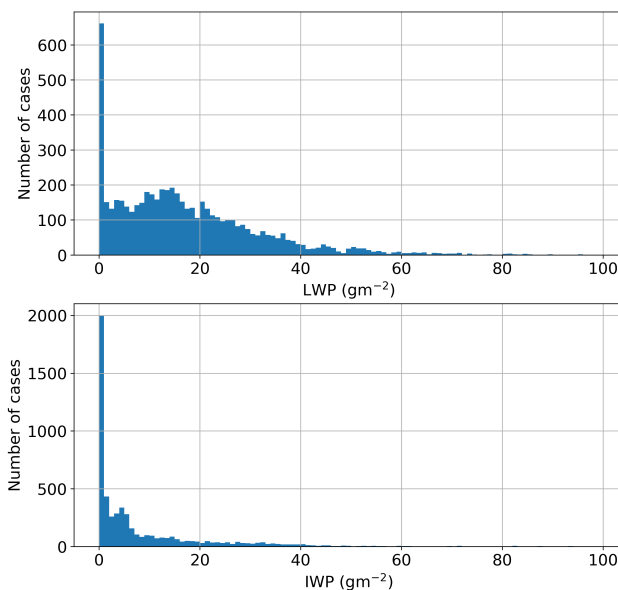
Figure 6. Distributin of retrieved LWP (upper plot) and IWP (lower plot).
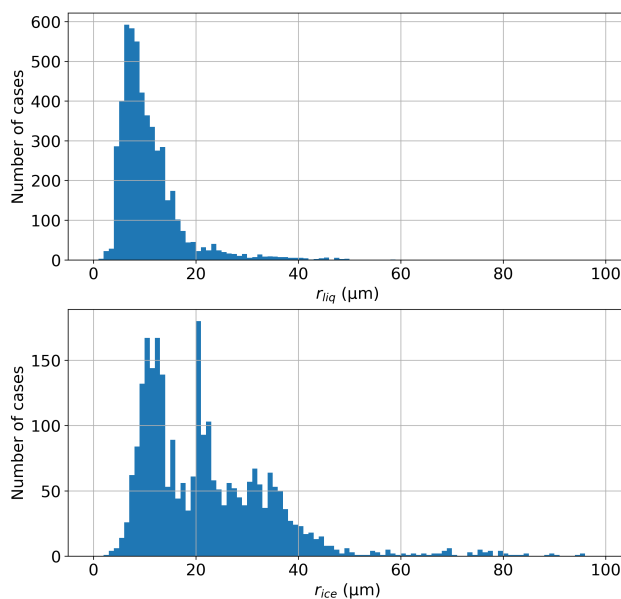
Figure 7. Distributin of retrieved effective radii for liquid water droplets (upper plot) and ice crystals (lower plot). In each case, only cases are considered in which the corresponding optical depths is above 0.1.

6 Results

6.1 Statistics of optical depths, effective radii and water paths

300

The dataset is published at Pangaea (Richter et al., 2021). During the measurement campaign, most of the observed optical depth is due to liquid water insted of ice crystals. A histogram of all retrieved optical depths is shown in figure (5). In 66.4 %

of the measurements, ice was observed in the clouds, whereas in 92.4% of the measurements liquid water was present. Mean optical depths are $\tau_{liq} = 2.64$ and $\tau_{ice} = 0.81$. Similar to the optical depth, most of the observed cloud water is liquid water

305 (figure 6). Here the means are $LWP = 17.68\,\mathrm{g \cdot m^{-2}}$ and $IWP = 9.92\,\mathrm{g \cdot m^{-2}}$. Interquartile ranges for LWP and IWP are $IQR_{LWP} = 18.90\,\mathrm{g \cdot m^{-2}}$ and $IQR_{IWP} = 11.53\,\mathrm{g \cdot m^{-2}}$. Whereas the range of LWP matches the LWP from the testcases, the IWP is near the lower threshold of the retrievable water path.

The distributions of the effective radii is shown in figure (7). For r_{liq} only cases with $f_{ice} < 0.9$ are used. Similar for r_{ice}, where only cases with $f_{ice} > 0.1$ are used. On average, ice crystals ($r_{ice} = 22.33\,\mu\mathrm{m}$) are larger than liquid droplets ($r_{liq} = $

310 $10.88\,\mu\mathrm{m}$). Ice crystals show a wider range of retrieved effective radii than liquid droplets, expressed by an interquartile range of $IQR_{ice} = 17.89\,\mu\mathrm{m}$ compared to $IQR_{liq} = 5.92\,\mu\mathrm{m}$.

6.2 Averaging Kernels

For all measurements, the mean of the averaging kernels and degrees of freedom are calculated:

$$\mathbf{A} = \begin{pmatrix} 0.77 & 0.48 & -0.17 & -0.02 \\ 0.19 & 0.45 & 0.25 & -0.01 \\ -0.04 & 0.14 & 0.74 & 0.05 \\ -0.03 & -0.1 & 0.29 & 0.3 \end{pmatrix} \tag{20}$$

315 $$tr(\mathbf{A}) = 2.25 \tag{21}$$

This mean averaging kernel matrix contains both single-phase clouds and mixed-phase clouds. Since only two parameters are determined in the single-phase cases, they perturb the mean number of degrees of freedom for all measurements. As seen in the statistics, there are less cases with ice-containing clouds. This also decreases the entries on the diagonals for τ_{ice} and r_{ice} as they are 0 in all-liquid clouds. Therefore, the mean averaging kernel was also calculated for all mixed-phase clouds:

320 $$\mathbf{A}_{mixed-phase} = \begin{pmatrix} 0.62 & 0.22 & -0.35 & -0.03 \\ 0.32 & 0.7 & 0.47 & -0.04 \\ -0.08 & 0.16 & 0.66 & 0.1 \\ -0.14 & -0.07 & 0.17 & 0.59 \end{pmatrix} \tag{22}$$

$$tr(\mathbf{A}_{mixed-phase}) = 2.57 \tag{23}$$

. The number of degrees of freedom in this case is 2.57. The entries for the effective radii are at the same size as those for the optical depth. However, one has to keep in mind that this averaging kernel has no information about the ice crystal shape. If the assumed shape of ice crystals is inappropriate, the result might be the correct size for the assumed ice crystal shape, but it

325 is not the real r_{ice} due to different geometries.
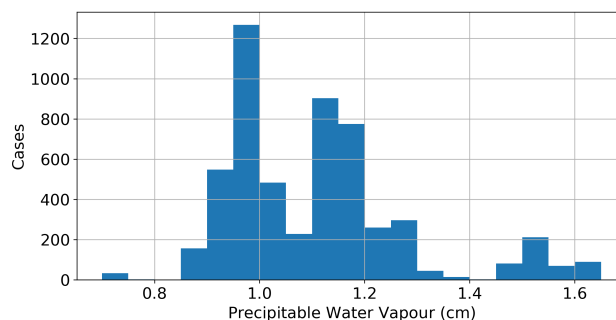
Figure 8. Statistics of the precipitable water vapour during the measurements of atmospheric radiances.
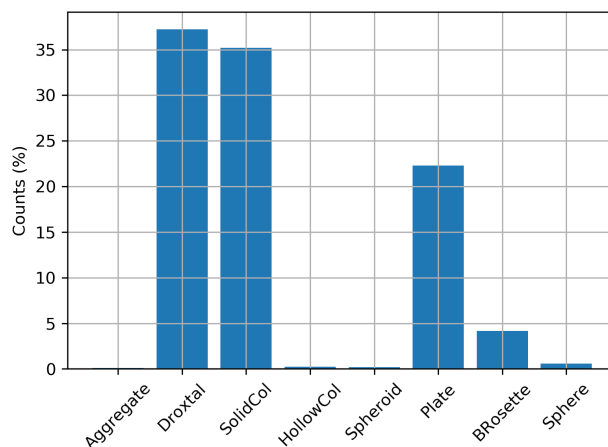
Figure 9. Percentage of retrievals, divided by the chosen ice particle shape. Most particles are modelled as droxtals (37 %), solid columns (35 %), plates (22 %) and bullet rosettes (4 %)

6.3 Precipitable water vapour

A crucial spectral region for the determination of the cloud phase are the spectral windows in the far-infrared between $500\,\mathrm{cm}^{-1}$ and $600\,\mathrm{cm}^{-1}$ (Rathke et al., 2002). This spectral region is sensitive to the concentration of water vapour in the atmosphere. The amount of water vapour is expressed by the precipitable water vapour PWV, which has been calculated from the radiosonde

330   measurements. The far-infrared spectral region becomes nearly intransparent to infrared radiation for PWV $> 1\,\mathrm{cm}$ (Cox et al., 2016). During the measurement campaign the PWV was greater than $1\,\mathrm{cm}$ in 62 % of the cases. Statistics of PWV are shown in figure (8).

Table 8. Results of the comparison between TCWret and Cloudnet for ice-related quantities. Mean gives TCWret minus Cloudnet.

Quantity	$\|r\|$	p-Value	Mean	STD
IWP	0.41	< 0.05	$1.54\,\mathrm{g\cdot m^{-2}}$	$16.69\,\mathrm{g\cdot m^{-2}}$
IWP ($PWV < 1\,\mathrm{cm}$)	0.31	< 0.05	$1.67\,\mathrm{g\cdot m^{-2}}$	$11.55\,\mathrm{g\cdot m^{-2}}$
r_{ice}	-0.04	> 0.05	$-16.77\,\mathrm{\mu m}$	$12.83\,\mathrm{\mu m}$

6.4 Comparison to Cloudnet

To compare result from TCWret and Cloudnet, a combined dataset of TCWret result is created in the following way: Where
335   r_{ice} is below $30\,\mathrm{\mu m}$, we used the result with ice crystals modelled as droxtals. If r_{ice} is above $30\,\mathrm{\mu m}$, we randomly chose the result retrieved using plates, solid columns or bullet rosette. Figure (9) shows the percentage of the used ice crystal shape in this new dataset. This choice is motivated by the ice crystal shapes described by Yang et al. (2007). As additional constraint, we only allow results where $r_{liq} < r_{ice}$. This is motivated the following: The results of r_{liq} and r_{ice} will show, that r_{liq} is usually smaller than r_{ice}. From the estimation of the retrieval performance using the testcases ans $\bar{r}$ can be seen, that an underestimated
340   r_{ice} comes with an overestimated r_{liq}. Therefore, cases with $r_{liq} > r_{ice}$ are likely cases with too small r_{ice} and too large r_{liq}. For the comparison between TCWret and Cloudnet, results from both datasets were averaged over a time period of two minutes. This has been done because the underlying measurement systems have different temporal resolutions, also both measurement systems were at different locations on the ship. Cloudnet results do not contain optical depths, but water paths and droplet radii, therefore we will compare LWP and IWP, r_{liq} and r_{ice}.

345   ### 6.4.1 Ice Water Path and ice effective radius

Results for the ice-related quantities are shown in table (8). For r_{ice}, no significant correlation between TCWret and Cloudnet could be found. In general, r_{ice} of TCWret is $16.77\,\mathrm{\mu m}$ smaller than r_{ice} from the Cloudnet retrieval. In contrast to the testcases where retrieval r_{ice} has been proven to be possible, the ice crystal geometry in the real measurements does not necessarily agree with the real ice shape. As seen in the study regarding the influence of the ice crystal geometry, an inappropriate geometry leads
350   to large uncertainties in the estimation of r_{ice}.

Figure (10) shows the results for the IWP. Although the IWP in TCWret is calculated from r_{ice}, a significant correlation between TCWret and Cloudnet can be observed. Withouth limiting the PWV, the difference between TCWret and Cloudnet is $(1.54 \pm 16.69)\,\mathrm{g\cdot m^{-2}}$ and with limiting the PWV to values below $1\,\mathrm{cm}$ the difference is $(1.67 \pm 11.55)\,\mathrm{g\cdot m^{-2}}$. As the mean
355   IWP in the measurements is $9.92\,\mathrm{g\cdot m^{-2}}$, the measurements are at the lower threshold of the detectable IWP from TCWret. This could be improved by external knowledge of the ice crystal geometry.
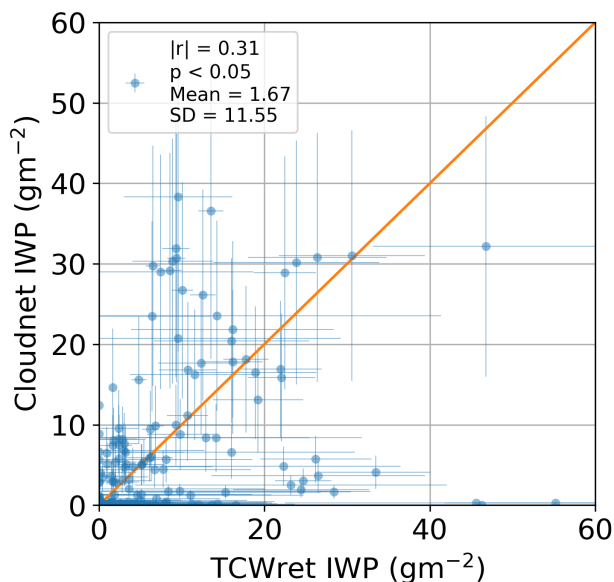
Figure 10. Ice water path of TCWret versus IWP from Cloudnet for $PWV < 1\,\mathrm{cm}$.

Table 9. Results of the comparison between TCWret and Cloudnet for liquid-related quantities. Mean gives TCWret minus Cloudnet.

Quantity	$|r|$	p-Value	Mean	STD
LWP	0.65	< 0.05	$2.48\,\mathrm{g\cdot m^{-2}}$	$10.13\,\mathrm{g\cdot m^{-2}}$
LWP $< 20\,\mathrm{g\cdot m^{-2}}$	0.52	< 0.05	$3.98\,\mathrm{g\cdot m^{-2}}$	$8.60\,\mathrm{g\cdot m^{-2}}$
LWP $(PWV < 1\,\mathrm{cm})$	0.73	< 0.05	$1.07\,\mathrm{g\cdot m^{-2}}$	$8.20\,\mathrm{g\cdot m^{-2}}$
LWP $< 20\,\mathrm{g\cdot m^{-2}}$ $(PWV < 1\,\mathrm{cm})$	0.72	< 0.05	$2.59\,\mathrm{g\cdot m^{-2}}$	$5.32\,\mathrm{g\cdot m^{-2}}$
r_{liq}	0.66	< 0.05	$4.40\,\mathrm{\mu m}$	$2.69\,\mathrm{\mu m}$
$r_{liq}\,(PWV < 1\,\mathrm{cm})$	0.47	< 0.05	$3.53\,\mathrm{\mu m}$	$2.35\,\mathrm{\mu m}$

6.4.2 Liquid Water Path and effective droplet radius

In table (9) the correlation coefficients, means and standard deviations for LWP and r_{liq} are shown. In the case of LWP, for
both the data with a limitation of the PWV to $1\,\mathrm{cm}$ and without this limitation a significant correlation of the results is ob-
360   served. Figure (11) (left side) shows the LWP from Cloudnet and TCWret for cases with PWV $< 1\,\mathrm{cm}$. The standard deviation
of $10.13\,\mathrm{g\cdot m^{-2}}$ for all cases and $8.20\,\mathrm{g\cdot m^{-2}}$ for the cases with PWV $< 1\,\mathrm{cm}$ is less than the mean error of the LWP from
Cloudnet $(20.40\,\mathrm{g\cdot m^{-2}})$.
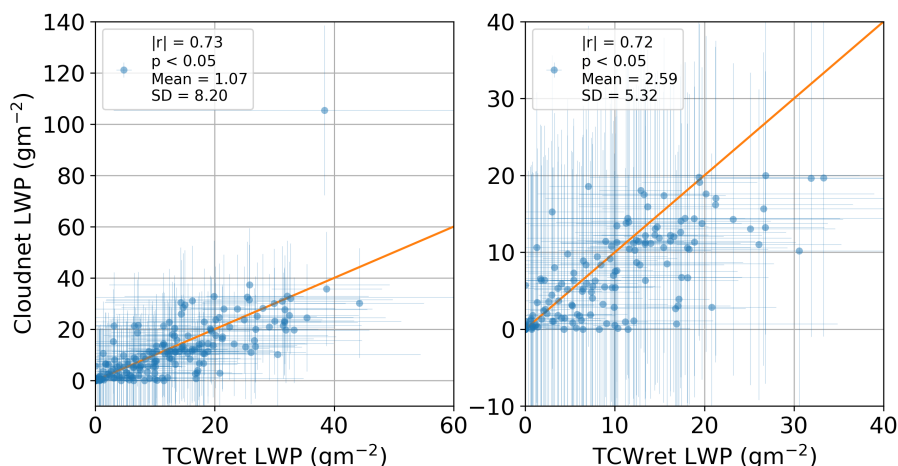
Figure 11. Liquid water path of TCWret versus Cloudnet for $PWV < 1\,\mathrm{cm}$. Left scatter plot contains all measurements, whereas the right plot only shows clouds with LWP $< 20\,\mathrm{g \cdot m^{-2}}$.
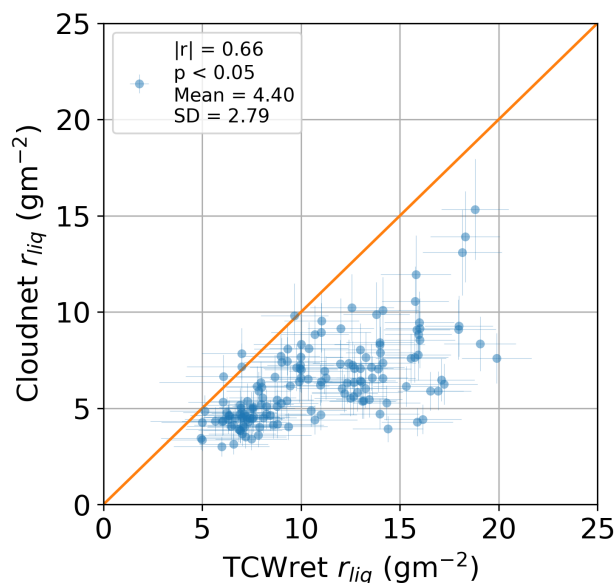
Figure 12. r_{liq} of TCWret versus r_{liq} from Cloudnet averaged over the entire cloud.

As seen, the standard deviation of the comparison is lower than those stated by Cloudnet for the individual measurement, so we will show how the results for very thin clouds are. Therefore clouds with LWP $< 20\,\mathrm{g \cdot m^{-2}}$ retrieved by Cloudnet will be

365   compared to LWP from TCWret. These results are below the uncertainty of Cloudnet, but as the standard deviation of the LWP for all clouds is below $20\,\mathrm{g \cdot m^{-2}}$, the comparison to TCWret allows an assessment of whether the Cloudnet-data is reliable for

very thin clouds during this measurement campaign. Results for very thin clouds (PWV $< 1\,\mathrm{cm}$) are shown in figure (11) (right side). Again, a signficiant correlation ($|r| = 0.72$) is observed. The standard deviation for these clouds is $5.32\,\mathrm{g} \cdot \mathrm{m}^{-2}$. From the comparison with TCWret, it can be concluded that during this measurement campaign, Cloudnet's results for thin clouds

370   with LWP $< 20\,\mathrm{g} \cdot \mathrm{m}^{-2}$ are also reliable despite the stated error of $20.40\,\mathrm{g} \cdot \mathrm{m}^{-2}$.

Figure (12) shows the results for r_{liq}. Only results from TCWret are considered if $f_{ice} < 0.9$. Accordingly, pure ice clouds are ignored. Overall, there is an overestimation of the r_{liq} of TCWret by $4.40\,\mathrm{\mu m}$ on average. The standard deviation is $2.79\,\mathrm{\mu m}$. A high PWV do not worsen the results of the retrieval. While the standard deviation is within the range of what would be expected

375   based on the testcases, the mean deviation is well above that from the testcases. This indicates that TCWret can determine the effective radius within the range of inaccuracies, but that there is a systematic effect that leads to an overestimation compared to r_{liq} of Cloudnet. To this end, refer to the mean effective radius $\bar{r} = (1 - f_{ice}) \cdot r_{liq} + f_{ice} \cdot r_{ice}$, which can be well determined by TCWret. In the previous section it was shown that TCWret underestimates r_{ice}. The large r_{liq} observed here is thus consistent with the small r_{ice} compared to Cloudnet: When real larger ice particles are identified as liquid droplets in the retrieval, r_{liq}

380   increases as r_{ice} decreases. Just like r_{ice}, r_{liq} thus improves if the ice crystal geometry was determined via other measurements.

7   Data availability

For accessability of used and shown datasets, see table (10).

8   Code availability

The retrieval algorithm TCWret is available at https://doi.org/10.5281/ZENODO.4621127 (Richter, 2021) with external sub-

385   routines at https://doi.org/10.5281/ZENODO.4618142 and https://doi.org/10.5281/ZENODO.4618106. Jupyer-Notebooks to perform the comparisons to Cloudnet are available at https://github.com/RichterIUP/evaluation_tcwret.

9   Summary and Conclusion

In this publication, a dataset of microphysical cloud parameters of optically thin clouds was presented. The measurements were carried out on the ship RV *Polarstern* in summer 2017 in the Arctic Ocean around Svalbard and in the Fram Strait.

390   Measurements were performed using a mobile FTIR spectrometer, operated in emission mode (EM-FTIR). A calibration of the EM-FTIR was performed with a blackbody radiator, whose temperature was alternately set to $100\,^{\circ}\mathrm{C}$ and ambient temperature. The spectrometer was operated in an air-conditioned container. Radiances between $500\,\mathrm{cm}^{-1}$ and $2000\,\mathrm{cm}^{-1}$ were recorded. The retrieval of cloud parameters was performed using the Total Cloud Water retrieval (TCWret). TCWret uses the optimal estimation method to invert atmospheric radiances. The radiative transfer model used is LBLDIS, which utilizes optical depths of

395   atmospheric trace gases calculated with LBLRTM and then calculates the spectral radiances using DISORT. Single-scattering parameters for clouds are read from pre-calculated databases. Retrieval products are the optical depths of water and ice and the

corresponding effective radii. TCWret also uses profiles of air pressure, humidity and temperature from measurements with Vaisala RS92 radiosondes and information about cloud height from measurements of the ceilometer CL51, which is on board the RV *Polarstern*.

400 Retrieval performance was tested using a dataset of testcases, containing examples of clouds typically observed in the Arctic. Using the correct ice particle shapes, TCWret is able to estimate optical depths, effective radii and water paths for liquid water and ice.

The comparison with the simultaneously performed retrievals of the Cloudnet network on the *Polarstern* shows:

- The LWP of both data sets are in agreement. In addition, it could be shown using the TCWret dataset that during this
405 measurement campaign also the measurement data of thin clouds (LWP $< 20 \, \mathrm{g \cdot m^{-2}}$) of the Cloudnet retrieval are reliable despite the given error of $20 \, \mathrm{g \cdot m^{-2}}$.

- A significant correlation for r_{liq} is observed, in contrast to r_{ice}. In the testcases r_{ice} could also be determined. However, the shape of the ice crystals was known there, in contrast to the ice crystals known during the measurement campaign. The effective radius of the ice crystals in TCWret is too small compared to Cloudnet. This affects r_{liq}, which is overestimated
410 compared to Cloudnet.

- The IWP can be determined despite the lack of information about the ice crystal shape. However, the IWP values during the measurement campaign are at the lower limit of what TCWret can determine based on the observed standard deviations.

In summary, the dataset of cloud parameters and water paths from TCWret provides a helpful complement to the results of
415 the LWP from Cloudnet, but at the same time benefits from its r_{liq}. Due to the consistent calculation of cloud parameters over the entire cruise, the results from TCWret additionally provide information about clouds during PS107, where only EM-FTIR measurements are available.

Author contributions. PR performed measurements during PS106 and PS107, implemented TCWret and retrieved from infrared spectra. MP designed and built the measurement setup, performed measurements during the PS106.1, measured the emissivity of the blackbody radiator
420 and gave advice in the development of TCWret. CW performed measurements during the PS106.2 and built the measurement setup. HG performed Cloudnet retrievals and gave advice in using the Cloudnet data. PMR gave advice in the application of the testcases. JN gave advice in the setup of the measurement and the development of TCWret. All authors contributed to manuscript revisions.

Competing interests. The authors declare no competing interests.

Acknowledgements. We gratefully acknowledge funding from the Deutsche Forschungsgemeinschaft (DFG, German Research Foundation,

425   TRR 172) - Projektnummer 268020496 - within the Transregional Collaborative Research Center - ArctiC Amplification: Climate Relevant
Atmospheric and SurfaCe Processes, and Feedback Mechanisms (AC)3 - in subproject B06 and E02. We thank the Alfred-Wegener-Institute
and RV *Polarstern* crew and captain for their support (AWI_PS106_00 and AWI_PS107_00). The computations were performed on the HPC
cluster Aether at the University of Bremen, financed by DFG within the scope of the Excellence Initiative.

References

430   Becker, E. and Notholt, J.: Intercomparison and validation of FTIR measurements with the Sun, the Moon and emission in the Arctic, Journal of Quantitative Spectroscopy and Radiative Transfer, 65, 779 – 786, https://doi.org/https://doi.org/10.1016/S0022-4073(99)00154-5, http://www.sciencedirect.com/science/article/pii/S0022407399001545, 2000.

Becker, E., Notholt, J., and Herber, A.: Tropospheric aerosol measurements in the Arctic by FTIR-emission and star photometer extinction spectroscopy, Geophysical Research Letters, 26, 1711–1714, https://doi.org/10.1029/1999GL900336, https://agupubs.onlinelibrary.wiley.
435   com/doi/abs/10.1029/1999GL900336, 1999.

Ceccherini, S. and Ridolfi, M.: Technical Note: Variance-covariance matrix and averaging kernels for the Levenberg-Marquardt solution of the retrieval of atmospheric vertical profiles, Atmospheric Chemistry and Physics, pp. 3131 – 3139, 2010.

Clough, S. A., Shephard, M. W., Mlawer, E. J., Delamere, J. S., Iacono, M. J., Cady-Pereira, K., Boukabara, S., and Brown, P. D.: Atmospheric radiative transfer modeling: a summary of the AER codes, Journal of Quantitative Spectroscopy & Radiative Transfer, 91, 233 – 244, 2005.

440   Cox, C. J., Rowe, P. M., Neshyba, S. P., and Walden, V. P.: A synthetic data set of high-spectral-resolution infrared spectra for the Arctic atmosphere, Earth System Science Data, 8, 199–211, https://doi.org/10.5194/essd-8-199-2016, https://www.earth-syst-sci-data.net/8/199/2016/, 2016.

Downing, H. D. and Williams, D.: Optical constants of water in the infrared, Journal of Geophysical Research (1896-1977), 80, 1656–1661, https://doi.org/10.1029/JC080i012p01656, https://agupubs.onlinelibrary.wiley.com/doi/abs/10.1029/JC080i012p01656, 1975.

445   Griesche, H., Seifert, P., Engelmann, R., Radenz, M., and Bühl, J.: Cloudnet IWC during PS106, https://doi.org/10.1594/PANGAEA.919452, https://doi.pangaea.de/10.1594/PANGAEA.919452, 2020a.

Griesche, H., Seifert, P., Engelmann, R., Radenz, M., and Bühl, J.: Cloudnet ice particles effective radius during PS106, https://doi.org/10.1594/PANGAEA.919386, https://doi.org/10.1594/PANGAEA.919386, 2020b.

Griesche, H., Seifert, P., Engelmann, R., Radenz, M., and Bühl, J.: Cloudnet LWC during PS106, https://doi.org/10.1594/PANGAEA.919383,
450   https://doi.org/10.1594/PANGAEA.919383, 2020c.

Griesche, H., Seifert, P., Engelmann, R., Radenz, M., and Bühl, J.: Cloudnet liquid droplet effective radius during PS106, https://doi.org/10.1594/PANGAEA.919399, https://doi.org/10.1594/PANGAEA.919399, 2020d.

Griesche, H. J., Seifert, P., Ansmann, A., Baars, H., Barrientos Velasco, C., Bühl, J., Engelmann, R., Radenz, M., Zhenping, Y., and Macke, A.: Application of the shipborne remote sensing supersite OCEANET for profiling of Arctic aerosols and clouds during *Polarstern* cruise
455   PS106, Atmospheric Measurement Techniques, 13, 5335–5358, https://doi.org/10.5194/amt-13-5335-2020, https://amt.copernicus.org/articles/13/5335/2020/, 2020e.

Hersbach, H., Bell, B., Berrisford, P., Biavati, G., Horányi, A., Muñoz Sabater, J., Nicolas, J., Peubey, C., Radu, R., Rozum, I., Schepers, D., Simmons, A., Soci, C., Dee, D., and Thépaut, J.-N.: ERA5 hourly data on pressure levels from 1979 to present. Copernicus Climate Change Service (C3S) Climate Data Store (CDS). (Accessed on 25-Sep-2020), https://doi.org/10.24381/cds.bd0915c6, 2018.

460   Illingworth, A. J., Hogan, R. J., O'Connor, E., Bouniol, D., Brooks, M. E., Delanoé, J., Donovan, D. P., Eastment, J. D., Gaussiat, N., Goddard, J. W. F., Haeffelin, M., Baltink, H. K., Krasnov, O. A., Pelon, J., Piriou, J.-M., Protat, A., Russchenberg, H. W. J., Seifert, A., Tompkins, A. M., van Zadelhoff, G.-J., Vinit, F., Willén, U., Wilson, D. R., and Wrench, C. L.: Cloudnet, Bulletin of the American Meteorological Society, 88, 883–898, https://doi.org/10.1175/BAMS-88-6-883, 2007.

Knuteson, R. O., Revercomb, H. E., Best, F. A., Ciganovich, N. C., Dedecker, R. G., Dirckx, T. P., Ellington, S. C., Feltz, W. F., Garcia, R. K.,
465   Howell, H. B., Smith, W. L., Short, J. F., and Tobin, D. C.: Atmospheric Emitted Radiance Interferometer. Part II: Instrument Performance,
Journal of Atmospheric and Oceanic Technology, 21, 1777–1789, https://doi.org/10.1175/JTECH-1663.1, 2004a.

Knuteson, R. O., Revercomb, H. E., Best, F. A., Ciganovich, N. C., Dedecker, R. G., Dirkx, T. P., Ellington, S. C., Feltz, W. F., Garcia, R. K.,
Howell, H. B., Smith, W. L., Short, J. F., and Tobin, D. C.: Atmospheric Emitted Radiance Interferometer. Part I: Instrument Design,
Journal of Atmospheric and Oceanic Technology, 21, 1763 – 1776, https://doi.org/10.1175/JTECH-1662.1, https://journals.ametsoc.org/
470   view/journals/atot/21/12/jtech-1662_1.xml, 2004b.

Löhnert, U. and Crewell, S.: Accuracy of cloud liquid water path from ground-based microwave radiometry 1. Dependency on cloud model
statistics, Radio Science, 38, https://doi.org/https://doi.org/10.1029/2002RS002654, https://agupubs.onlinelibrary.wiley.com/doi/abs/10.
1029/2002RS002654, 2003.

Macke, A. and Flores, H.: The Expeditions PS106/1 and 2 of the Research Vessel POLARSTERN to the Arctic Ocean in 2017,
475   https://doi.org/10.2312/BzPM_0719_2018, 2018.

Rathke, C. and Fischer, J.: Retrieval of Cloud Microphysical Properties from Thermal Infrared Observations by a Fast Itera-
tive Radiance Fitting Method, Journal of atmospheric and oceanic technology, 17, 1509 – 1524, https://doi.org/10.1175/1520-
0426(2000)017<1509:ROCMPF>2.0.CO;2, 2000.

Rathke, C., Fischer, J., Neshyba, S., and Shupe, M.: Improving IR cloud phase determination with 20 microns spectral observations, Geo-
480   physical Research Letters, pp. 51 – 54, https://doi.org/10.1029/2001GL014594, 2002.

Revercomb, H. E., Buijs, H., Howell, H. B., Laporte, D. D., Smith, W. L., and Sromovsky, L. A.: Radiometric calibration of IR Fourier
transform spectrometers: solution to a problem with the High-Resolution Interferometer Sounder, Applied Optics, 27, 3210 – 3218,
https://doi.org/10.1364/AO.27.003210, 1988.

Richter, P.: Total Cloud Water retrieval, https://doi.org/10.5281/zenodo.4621127, https://doi.org/10.5281/zenodo.4621127, 2021.

485 Richter, P., Palm, M., Weinzierl, C., and Notholt, J.: Microphysical Cloud Parameters and water paths retrieved from EM-FTIR spectra,
measured during PS106 and PS107 in Arctic summer 2017, https://doi.pangaea.de/10.1594/PANGAEA.933829, 2021.

Rodgers, C.: Inverse Methods for Atmospheric Sounding: Theory and Practice, World Scientific, https://doi.org/10.1142/3171, 2000.

Rowe, P. M., Neshyba, S., and Walden, V. P.: Radiative consequences of low-temperature infrared refractive indices for super-
cooled water clouds, Atmospheric Chemistry and Physics, 13, 11 925–11 933, https://doi.org/10.5194/acp-13-11925-2013, https://www.
490   atmos-chem-phys.net/13/11925/2013/, 2013.

Rowe, P. M., Cox, C. J., Neshyba, S., and Walden, V. P.: Toward autonomous surface-based infrared remote sensing of polar clouds: retrievals
of cloud optical and microphysical properties, Atmospheric Measurement Techniques, 12, 5071–5086, https://doi.org/10.5194/amt-12-
5071-2019, https://www.atmos-meas-tech.net/12/5071/2019/, 2019.

Schewe, I.: The Expedition PS107 of the Research Vessel POLARSTERN to the Fram Strait and the AWI-HAUSGARTEN in 2017,
495   https://doi.org/10.2312/BzPM_0717_2018, 2018.

Schmithüsen, H.: Ceilometer CL51 raw data measured during POLARSTERN cruise PS106.1, links to files,
https://doi.org/10.1594/PANGAEA.883320, https://doi.org/10.1594/PANGAEA.883320, 2017a.

Schmithüsen, H.: Ceilometer CL51 raw data measured during POLARSTERN cruise PS106.2, links to files,
https://doi.org/10.1594/PANGAEA.883322, https://doi.org/10.1594/PANGAEA.883322, 2017b.

500 Schmithüsen, H.: Ceilometer CL51 raw data measured during POLARSTERN cruise PS107, links to files,
https://doi.org/10.1594/PANGAEA.883323, https://doi.org/10.1594/PANGAEA.883323, 2017c.

Schmithüsen, H.: Upper air soundings during POLARSTERN cruise PS106.1 (ARK-XXXI/1.1), https://doi.org/10.1594/PANGAEA.882736, https://doi.org/10.1594/PANGAEA.882736, 2017d.

Schmithüsen, H.: Upper air soundings during POLARSTERN cruise PS106.2 (ARK-XXXI/1.2), https://doi.org/10.1594/PANGAEA.882843, https://doi.org/10.1594/PANGAEA.882843, 2017e.

Schmithüsen, H.: Upper air soundings during POLARSTERN cruise PS107 (ARK-XXXI/2), https://doi.org/10.1594/PANGAEA.882889, https://doi.org/10.1594/PANGAEA.882889, 2017f.

Shupe, M. and Intrieri, J.: Cloud Radiative Forcing of the Arctic Surface: The Influence of Cloud Properties, Surface Albedo, and Solar Zenith Angle, Journal of Climate, 17, 616 – 628, https://doi.org/10.1175/1520-0442(2004)017<0616:CRFOTA>2.0.CO;2, 2004.

Stamnes, K., Tsay, S. C., Wiscombe, W., and Jayaweera, K.: Numerically stable algorithm for discrete-ordinate-method radiative transfer in multiple scattering and emitting layered media, Applied Optics, 27, 2502 – 2509, 1988.

Turner, D. D.: Arctic Mixed-Phase Cloud Properties from AERI Lidar Observations: Algorithm and Results from SHEBA, Americal Meteorological Society, pp. 427 – 444, 2005.

Turner, D. D.: Additional Information for LBLDIS, https://www.nssl.noaa.gov/users/dturner/public_html/lbldis/index.html, 2014.

Turner, D. D., Vogelmann, A. M., Baum, B. A., Revercomb, H. E., and P., Y.: Cloud Phase Determination Using Ground-Based AERI Observations at SHEBA, Americal Meteorological Society, pp. 701 – 715, 2003.

Turner, D. D., Vogelmann, A. M., Austin, R. T., Barnard, J. C., Cady-Pereira, K., Chiu, J. C., Clough, S. A., Flynn, C., Khaiyer, M. M., Liljegren, J., Johnson, K., Lin, B., Long, C., Marshak, A., Matrosov, S. Y., McFarlane, S. A., Miller, M., Min, Q., Minnis, P., O'Hirok, W., Wang, Z., and Wiscombe, W.: Thin Liquid Water Clouds - Their Importance and Our Challenge, Americal Meteorological Society, pp. 177 – 190, https://doi.org/10.1175/BAMS-88-2-I77, 2007.

Warren, S. G.: Optical constants of ice from the ultraviolet to the microwave, Appl. Opt., 23, 1206–1225, https://doi.org/10.1364/AO.23.001206, http://ao.osa.org/abstract.cfm?URI=ao-23-8-1206, 1984.

Wendisch, M., Macke, A., Ehrlich, A., Lüpkes, C., Mech, M., Chechin, D., Dethloff, K., Velasco, C. B., Bozem, H., Brückner, M., Clemen, H.-C., Crewell, S., Donth, T., Dupuy, R., Ebell, K., Egerer, U., Engelmann, R., Engler, C., Eppers, O., Gehrmann, M., Gong, X., Gottschalk, M., Gourbeyre, C., Griesche, H., Hartmann, J., Hartmann, M., Heinold, B., Herber, A., Herrmann, H., Heygster, G., Hoor, P., Jafariserajehlou, S., Jäkel, E., Järvinen, E., Jourdan, O., Kästner, U., Kecorius, S., Knudsen, E. M., Köllner, F., Kretzschmar, J., Lelli, L., Leroy, D., Maturilli, M., Mei, L., Mertes, S., Mioche, G., Neuber, R., Nicolaus, M., Nomokonova, T., Notholt, J., Palm, M., van Pinxteren, M., Quaas, J., Richter, P., Ruiz-Donoso, E., Schäfer, M., Schmieder, K., Schnaiter, M., Schneider, J., Schwarzenböck, A., Seifert, P., Shupe, M. D., Siebert, H., Spreen, G., Stapf, J., Stratmann, F., Vogl, T., Welti, A., Wex, H., Wiedensohler, A., Zanatta, M., and Zeppenfeld, S.: The Arctic Cloud Puzzle: Using ACLOUD/PASCAL Multiplatform Observations to Unravel the Role of Clouds and Aerosol Particles in Arctic Amplification, Bulletin of the American Meteorological Society, 100, 841–871, https://doi.org/10.1175/BAMS-D-18-0072.1, https://doi.org/10.1175/BAMS-D-18-0072.1, 2019.

Yang, P., Gao, B.-C., Baum, B. A., Hu, Y. X., Wiscombe, W. J., Tsay, S.-C., Winker, D. M., and Nasiri, S. L.: Radiative properties of cirrus clouds in the infrared (8–13um) spectral region, Journal of Quantitative Spectroscopy and Radiative Transfer, 70, 473–504, https://doi.org/https://doi.org/10.1016/S0022-4073(01)00024-3, https://www.sciencedirect.com/science/article/pii/S0022407301000243, light Scattering by Non-Spherical Particles, 2001.

Yang, P., Zhang, L., Hong, G., Nasiri, S. L., Baum, B. A., Huang, H., King, M. D., and Platnick, S.: Differences Between Collection 4 and 5 MODIS Ice Cloud Optical/Microphysical Products and Their Impact on Radiative Forcing Simulations, IEEE Transactions on Geoscience and Remote Sensing, 45, 2886–2899, https://doi.org/10.1109/TGRS.2007.898276, 2007.

540   Zasetsky, A. Y., Khalizov, A. F., Earle, M. E., and Sloan, J. J.: Frequency Dependend Complex Refractive Indices of Super-cooled Liquid Water and Ice Determined from Aerosol Extinction Spectra, Journal of Physical Chemistry A, pp. 2760 – 2764, https://doi.org/10.1021/jp044823c, 2005.

Table 10. Datasets used in this publication.

Description	DOI	Citation
Microphysical Cloud Parameters from TCWret	https://doi.pangaea.de/10.1594/PANGAEA.933829	Richter et al. (2021)
Cloudnet IWC during PS106	https://doi.org/10.1594/PANGAEA.919452	Griesche et al. (2020a)
Cloudnet r_{ice} during PS106	https://doi.org/10.1594/PANGAEA.919386	Griesche et al. (2020b)
Cloudnet LWC during PS106	https://doi.org/10.1594/PANGAEA.919383	Griesche et al. (2020c)
Cloudnet r_{liq} during PS106	https://doi.org/10.1594/PANGAEA.919399	Griesche et al. (2020d)
Ceilometer CL51 raw data measured during POLARSTERN cruise PS106.1	https://doi.org/10.1594/PANGAEA.883320	Schmithüsen (2017a)
Ceilometer CL51 raw data measured during POLARSTERN cruise PS106.2	https://doi.org/10.1594/PANGAEA.883322	Schmithüsen (2017b)
Ceilometer CL51 raw data measured during POLARSTERN cruise PS107	https://doi.org/10.1594/PANGAEA.883323	Schmithüsen (2017c)
Upper air soundings during POLARSTERN cruise PS106.1 (ARK-XXXI/1.1)	https://doi.org/10.1594/PANGAEA.882736	Schmithüsen (2017d)
Upper air soundings during POLARSTERN cruise PS106.2 (ARK-XXXI/1.2)	https://doi.org/10.1594/PANGAEA.882743	Schmithüsen (2017e)
Upper air soundings during POLARSTERN cruise PS107 (ARK-XXXI/2)	https://doi.org/10.1594/PANGAEA.882789	Schmithüsen (2017f)